

# We are IntechOpen, the world's leading publisher of Open Access books Built by scientists, for scientists

4,800

Open access books available

122,000

International authors and editors

135M

Downloads

Our authors are among the

154

Countries delivered to

TOP 1%

most cited scientists

12.2%

Contributors from top 500 universities



WEB OF SCIENCE™

Selection of our books indexed in the Book Citation Index  
in Web of Science™ Core Collection (BKCI)

Interested in publishing with us?  
Contact [book.department@intechopen.com](mailto:book.department@intechopen.com)

Numbers displayed above are based on latest data collected.  
For more information visit [www.intechopen.com](http://www.intechopen.com)



# Computational modelling of conduction mode laser welding process

S. Bag<sup>1</sup> and A. De<sup>2</sup>

<sup>1</sup>*CEMEF-Mines ParisTech, 06904 Sophia Antipolis Cedex, France*

<sup>2</sup>*IIT Bombay, Powai, Mumbai 400076 India*

## 1. Introduction

Laser welding has the advantage of localised heat, low distortion and rapid solidification, and is used in wide variety of material joining applications. Laser welding is performed either in conduction or in keyhole mode. In conduction mode, the applied power density is smaller and vaporization of work piece material is absent. Keyhole mode laser welding involves the application of very high power density creating a vapour filled cavity into the work piece that also helps in greater absorption of beam energy (Benyounis et al., 2005; Liu et al., 1993; Tzeng, 1999). An appropriate design for welding procedure requires a-priori knowledge of the peak temperature, weld thermal cycle and cooling rate. Due to high peak temperature and small weld pool size, real-time measurements of temperature and velocity fields, and the growth of weld pool are difficult in laser welding (DeRoy & David, 1995; Zhao et al., 1999; Pitscheneder et al., 1997; Lhospitalier et al., 1999; Lee & Kim, 2004). Thus, the computational models, which can simulate temperature and velocity field in laser welding, is in ever demand.

Conduction heat transfer based models are simpler, computationally inexpensive and yet can provide fairly reliable results in several simple welding systems (Trivedi et al., 2007; Goldak et al., 1984; Frewin & Scott, 1999; De et al., 2003). The transport phenomena based heat transfer and fluid flow analysis involves larger physical attributes, generally complex and can be computationally expensive especially for large and complex weld joint geometry (Bag & De, 2008; Bag & De, 2009; Mackwood & Crafer, 2005). Thus, conduction heat transfer based models are often preferred to the convective heat transport based weld pool simulations for smaller weld pool sizes and joining processes involving rapid melting and solidification. The conduction heat transfer based weld pool models also find tremendous application in the calculations of weld distortion and residual stress (Teng et al., 2001; Jung & Tsai, 2004; Deng et al., 2007; Cho & Kim, 2002; Trivedi et al., 2007; Deng, 2009), where the temperature field over a very large domain is of greater importance in comparison to its local variation in weld pool. We present here both of these modelling approaches and a comparison of the relative error in respective predictions.

In both the conduction and convective transport based models, the laser beam is considered as a surface heat source with Gaussian energy distribution. In conduction based heat transfer analysis, a volumetric heat source is often used further to numerically compensate the influence of convection heat transport in weld pool. The existing approach to define a volumetric heat source needs a-priori definition of its shape and size that restricts the use of the same (Goldak et al., 1984; Frewin & Scott, 1999; De et al., 2003). We have introduced an adaptive volumetric heat source term to make it more general and close to the reality. The adaptive volumetric term is defined by mapping the instantaneous value of the computed weld dimensions (length, width and depth) with respect to time step (transient) or load step (steady-state) and thus, the requirement of a-priori definition of the source geometry is avoided. Lastly, both conduction and convective heat transport based simulations of laser welding needs a number of parameters, which are required for model calculations and cannot be defined by scientific principles alone. Absorption coefficient, effective thermal conductivity and viscosity of molten material in weld pool, and parameter defining the nature of energy distribution are examples of such parameters in laser welding simulations (Chande & Mazumder, 1984; Tanriver et al., 2000; De & DebRoy, 2005). Here we show that a robust optimization algorithm integrated with the numerical process models can help in identifying suitable values of the uncertain model parameters and provide reliable computed results.

The present work includes a finite element based three-dimensional transient and quasi-steady heat transfer and fluid flow model for the prediction of temperature and velocity field, and weld dimensions in laser welding process. The novel feature introduced in the conduction model is the adaptive volumetric heat source term that is used to account for the energy absorbed by the molten weld pool in conduction based analysis. Temperature dependent material properties and the latent heat of melting and solidification are considered. The transport phenomena based heat transfer and fluid flow model considers effective values of thermal conductivity and viscosity to account for the effect of high momentum transport within small weld pool. The numerical heat transfer models are integrated with a differential evolution (DE) based optimization tool to estimate the value of uncertain parameters in an inverse manner. The predicted weld pool dimensions from the overall integrated model are validated successfully against similar experimentally measured results for laser spot and linear welding. The comparative results in terms of weld pool shape and size for both conduction and transport phenomena based models are presented.

## 2. Finite element based numerical model

The finite element formulation of 3D conduction mode heat transfer model using adaptive volumetric heat source both for spot and linear welding is described first. The discretization of transport phenomena based heat transfer and fluid flow model is presented next. Various issues regarding computational difficulties are also pointed out in this section.

### 2.1 Heat transfer model with adaptive volumetric heat source

The conduction mode heat transfer in transient state is governed by the following equation in 3D Cartesian coordinate system.

$$\frac{\partial}{\partial x_m} \left( k \frac{\partial T}{\partial x_m} \right) + \dot{Q} = \rho C_p \frac{\partial T}{\partial t} \quad (1)$$

where  $x_m$  is the distance along the  $m = 1, 2$  and  $3$  (same as  $x, y$  and  $z$ ) orthogonal directions and  $\rho, C_p$  and  $k$  refer respectively to density, and temperature dependent specific heat and thermal conductivity of the work piece material. The term  $\dot{Q}$  refers to the rate of internal heat generation per unit volume and  $t$  refers to time variable. Physically, the internal heat generation due to joule heating is neglected in the present model. However the volumetric heat source is mathematically incorporated through the term  $\dot{Q}$ . In steady state analysis, the transient growth of temperature field is transformed to special distribution by considering that the laser beam is moving with a constant velocity ( $V_w$ ) (say, in  $x_2$  i.e.  $y$ -direction). Hence, eq. (1) is rewritten for moving heat source with reference to the moving coordinate system ( $x_1, x_2, x_3$ ) as

$$\frac{\partial}{\partial x_m} \left( k \frac{\partial T}{\partial x_m} \right) + \dot{Q} = -\rho C_p \left( -V_w \frac{\partial T}{\partial x_2} \right) \quad (2)$$

It is to be noted from the nature of eq. (2) that the temperature is distributed specially and it is termed as quasi-steady state analysis. The boundary interaction along with the solution domain is described in Fig. 1. Mathematically, the heat balance along with the surface is expressed as

$$-k \frac{\partial T}{\partial n} = Q_c + Q_r - Q_s \quad (3)$$

where  $Q_c$  and  $Q_r$  represent heat loss by convection and radiation from the surface, respectively, and  $Q_s$  is the heat flux added by laser on the surface. The first term in eq. (2) indicates the heat conducted normal to the surface. On the symmetric surface, the temperature gradient normal to the surface is zero. The initial temperature of whole solution domain is considered as ambient temperature ( $T_0$ ). To avoid the computational difficulty of the radiation term, an effective heat transfer coefficient (combined effect of convection and radiation) is considered as (Frewin & Scott, 1999)

$$h_{\text{eff}} = 2.4 \cdot 10^{-3} \cdot \varepsilon \cdot T^{1.61} \quad (4)$$

where  $\varepsilon$  is the emissivity of the work piece material. Hence, the convection and radiation term of eq. (3) is expressed in modified form as

$$Q_{c'} = Q_c + Q_r = h_{\text{eff}} (T - T_0) \quad (5)$$

The distribution of laser energy on the top surface follows Gaussian distribution which is mathematically expressed as (Goldak et al., 1984)

$$Q_s = \frac{P\eta_c d_1}{\pi r_{\text{eff}}^2} \exp\left(-\frac{d_1}{r_{\text{eff}}^2} \sum_{m=1}^2 x_m^2\right) \quad (6)$$

where  $P$  refers to laser power,  $\eta_c$  and  $r_{\text{eff}}$  the absorption coefficient and effective radius of laser beam on the work piece surface, respectively, and  $d_1$  the power density distribution factor of heat source. Figure 2 describes the typical simulation of laser heat flux distribution on the substrate surface. The nature of distribution with respect to maximum heat flux is mainly extended by the distribution factor ( $d_1$ ) which is typically  $\sim 3.5$  for laser welding process (Frewin & Scott, 1999).

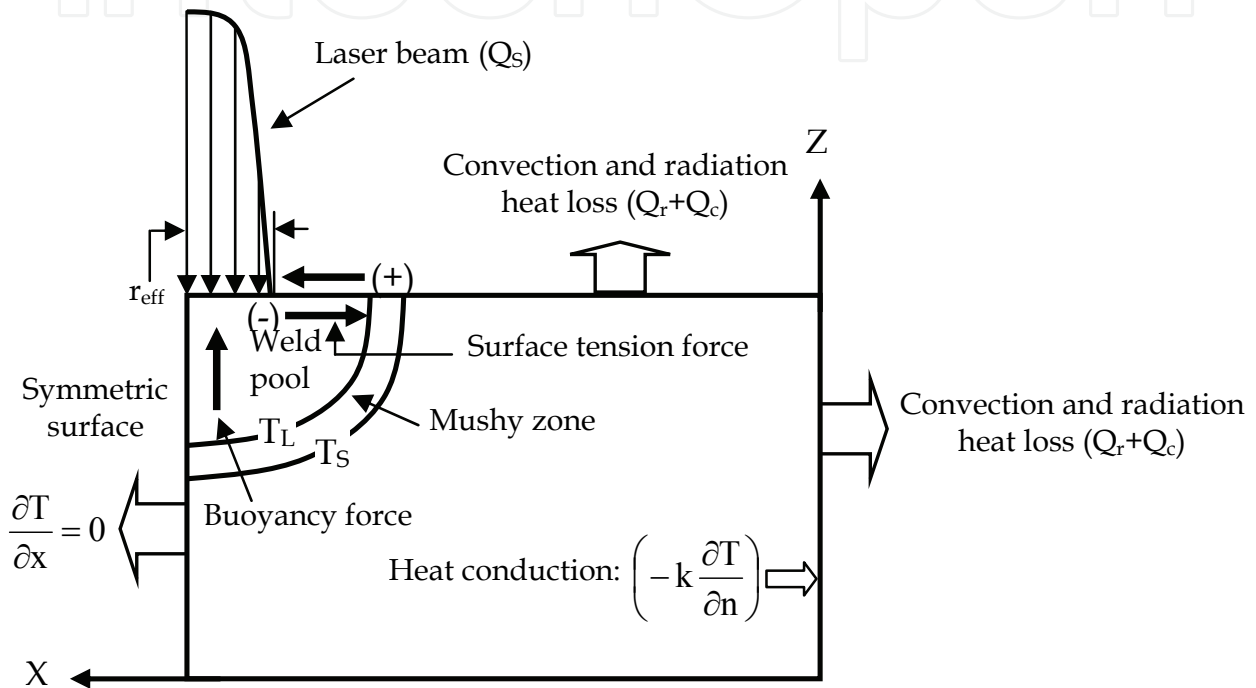


Fig. 1. Boundary conditions applied in numerical modelling of laser welding process.

Figure 3 schematically represents the shape of the volumetric heat source and it is mathematically represented as

$$\dot{Q} = \frac{6\sqrt{3}fP\eta_v}{\pi\sqrt{\pi} a_1 a_2 a_3} \exp\left(-3\sum_{m=1}^3 \frac{x_m^2}{a_m^2}\right) \quad (7)$$

where  $a_1$ ,  $a_2$  and  $a_3$  represent the computed values of the weld dimensions obtained iteratively after every time-step or load-step, and  $\eta_v$  refers to volumetric efficiency. The volumetric efficiency dictates the actual amount of volumetric heat that is utilised to develop the weld pool. The distribution of heat is uneven in the case of moving heat source (linear welding). The convective transport in weld pool gets lesser time to develop in the front of the heat source in comparison to the rear resulting in an asymmetric weld pool with respect to the centre of the source in the direction of weld velocity. In stationary welding, however, the weld pool remains symmetric owing to a symmetric energy distribution. To

incorporate the asymmetric effect in linear welding, eq. (7) is multiplied with an empirical constant  $f$  with  $f = 0.6$  for the front and  $1.4$  for the rear of the weld pool (Bonifaz, 2000) with the dimensions of double ellipsoidal  $2a_1$ ,  $a_3$ ,  $a_2^1$  and  $a_2^2$  ( $a_2 = a_2^1 + a_2^2$  and  $a_2^1 < a_2^2$ ) as shown in Fig. 3(a). In laser spot welding,  $f$  remains as unity with a symmetrical pool shape with respect to the centre of the heat source (Fig.3b).

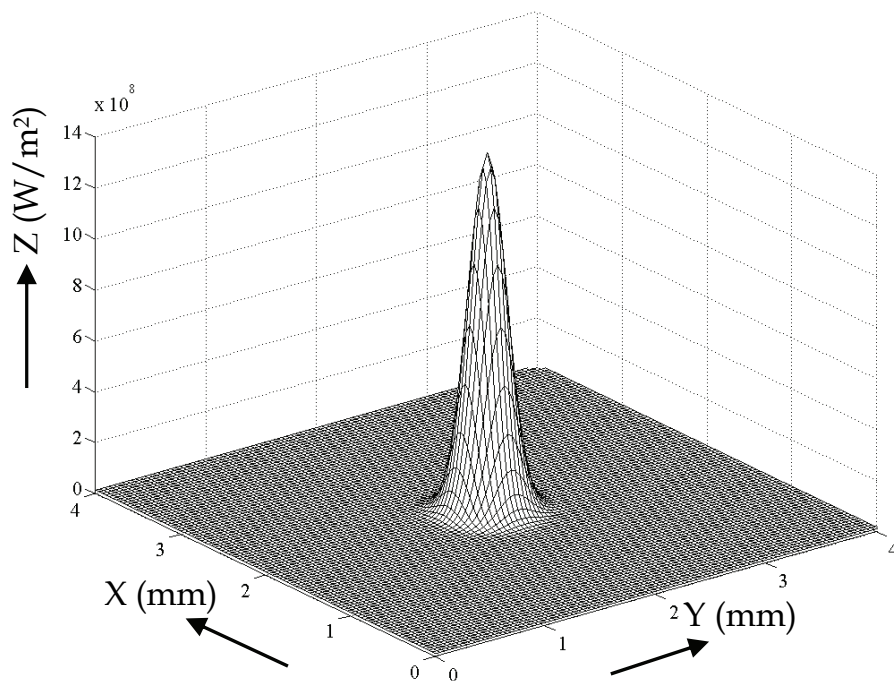


Fig. 2. Distribution of surface heat flux on work piece following Gaussian distribution.

The numerical calculations are performed through a number of small load steps in steady state analysis (linear welding) and time steps for transient analysis (spot welding). These small steps facilitate incorporation of the temperature dependence of materials properties through iterative procedures. The volumetric heat source term is activated when a finite size of molten weld pool forms. A direct iteration scheme is adopted to get a converged solution of temperature field by minimizing the error between the adaptive weld pool size of current load step and the previous load step.

The solution domain is discretized using eight noded isoparametric element with linear variation of temperature. The temperature variable,  $T$ , within the element is expressed in terms of nodal temperatures as

$$T = \sum_{i=1}^8 [N_i] \{T_i\} \quad (8)$$

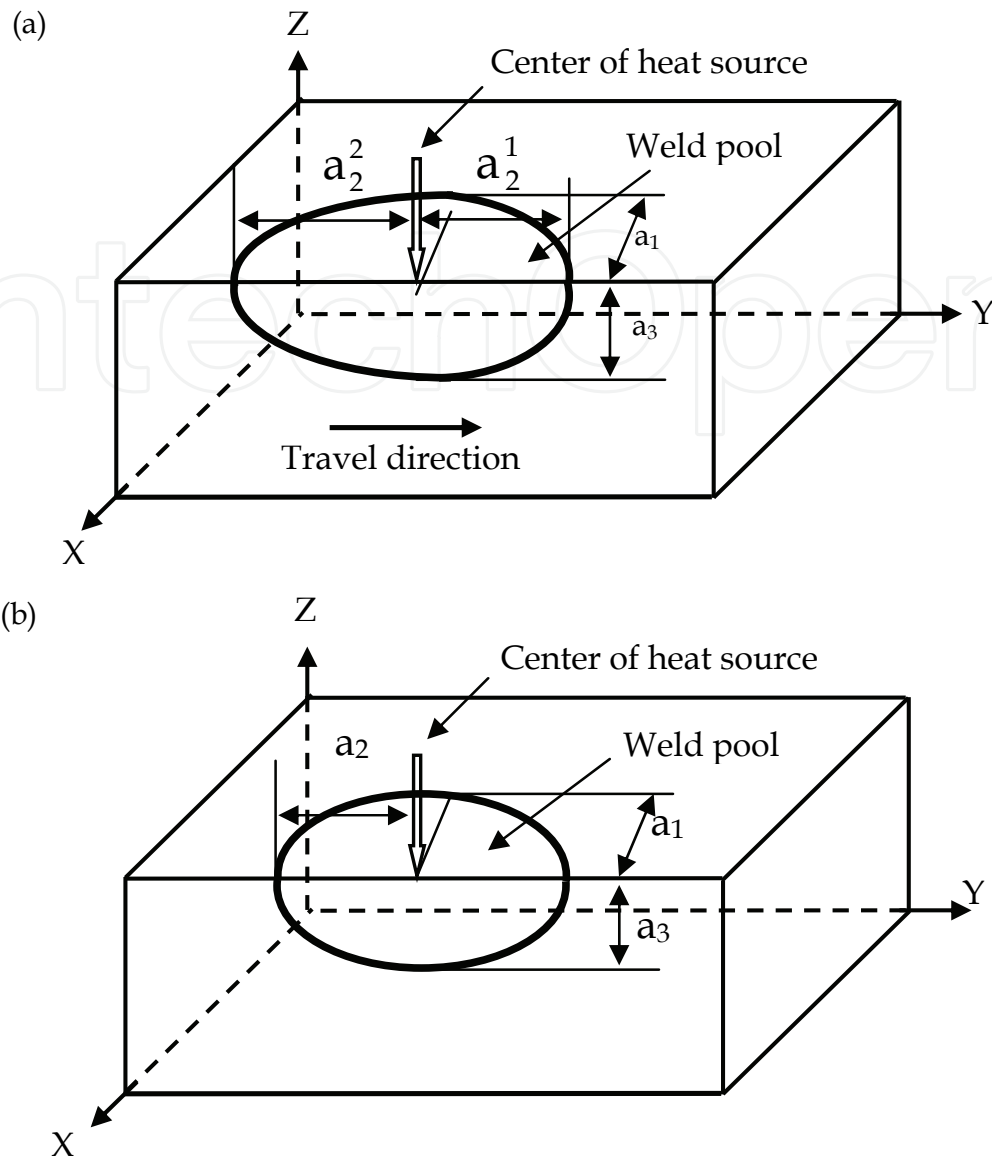


Fig. 3. Adaptive volumetric heat source in (a) linear welding and (b) transient spot welding.

The governing equation along with the boundary conditions is discretised with Galerkin's weighted residue technique (Gupta, 2002). By using Gauss theorem and boundary conditions described in eq. (3), the discretised form of the governing equation can be rewritten in matrix form for any specific element 'e' as

$$[K^e] \{T\} + [S^e] \left\{ \frac{\partial T}{\partial t} \right\} + [H^e] \{T\} - \{F_v^e\} - \{F_s^e\} - \{F_c^e\} = 0 \quad (9)$$

where

$$[K^e] = \int_{\Omega} k \sum_{m=1}^3 \left( \frac{\partial N_i}{\partial x_m} \frac{\partial N_j}{\partial x_m} \right) d\Omega \quad (10)$$

$$[S^e] = \int_{\Omega} \rho C_p N_i N_j d\Omega ; \quad [H^e] = \int_{\Gamma} h_{\text{eff}} N_i N_j d\Gamma \quad (11, 12)$$

$$\{F_s^e\} = \int_{\Gamma_i} N_i Q_s d\Gamma ; \{F_c^e\} = \int_{\Gamma_i} N_i h_{eff} T_0 d\Gamma \quad (13, 14)$$

$$\{F_v^e\} = \int_{\Omega} N_i \dot{Q} d\Omega \quad (15)$$

$$i, j = 1, 2, 3, 4, 5, 6, 7, 8 \quad \text{for 8 noded brick element} \quad (16)$$

Here,  $[K^e]$  represents the overall heat conduction within solution domain,  $[S^e]$  represents the heat capacity of domain,  $[H^e]$  defines the heat loss by convection and radiation from the surface, and  $\{F_s^e\}$ ,  $\{F_v^e\}$  and  $\{F_c^e\}$  represent heat added by laser beam through surface, volumetric heat added to the domain, and heat added through surface due to reference temperature, respectively. Considering the contribution from all the elements, the final set of equation in matrix form is written as

$$[\bar{K}]\{T\} + [S]\left\{\frac{\partial T}{\partial t}\right\} = \{F\} \quad (17)$$

where

$$[\bar{K}] = [K] + [H] ; \{F\} = \{F_v\} + \{F_s\} + \{F_c\} \quad (18, 19)$$

However, to get the temperature distribution over time, eq. (17) is further discretised linearly in the time domain following Galerkin's scheme which is unconditionally stable (Reddy & Gartling, 2000). Assuming that the temperature field at the beginning of the time interval,  $\Delta t$ , is known, the same at the end of the time interval is calculated as

$$\{T^2\} = -\left[\frac{2}{3}[\bar{K}] + \frac{1}{\Delta t}[S]\right]^{-1} \left\{\left[\frac{1}{3}[\bar{K}] - \frac{1}{\Delta t}[S]\right]\{T^1\} - \{F\}\right\} \quad (20)$$

In similar fashion, the matrix form of the equation for pseudo-steady state heat transfer analysis can be written as

$$[K^e]\{T\} + [S^e]\{T\} + [H^e]\{T\} = \{F_v^e\} + \{F_s^e\} + \{F_c^e\} \quad (21)$$

where

$$[S^e] = -\int_{\Omega} \rho C_p V_w N_i \frac{\partial N_i}{\partial x_2} d\Omega \quad (22)$$

The expressions of other terms are already described in transient heat transfer analysis. Considering the contribution from all the elements within the solution domain the final set of equation for pseudo-steady state heat transfer analysis is expressed as

$$[\bar{K}]\{T\} = \{F\} \quad (23)$$

where

$$[\bar{K}] = [K] + [S] + [H] ; \{F\} = \{F_v\} + \{F_s\} + \{F_c\} \quad (24, 25)$$



## 2.2 Transport phenomena based heat transfer and fluid flow model

In addition to the energy equation, heat transfer and fluid flow analysis requires the solution of the momentum conservation equation expressed as (Reddy & Gartling, 2000)

$$\rho \left( \frac{\partial \mathbf{u}_m}{\partial t} + \mathbf{u}_n \frac{\partial \mathbf{u}_m}{\partial x_n} \right) = F_m + \frac{\partial}{\partial x_m} \left[ -P\delta_{mn} + \mu_{\text{eff}} \left( \frac{\partial \mathbf{u}_m}{\partial x_n} + \frac{\partial \mathbf{u}_n}{\partial x_m} \right) \right] \quad (26)$$

where  $\mathbf{u}_m$  is the velocity in respective direction and  $m, n = 1, 2, 3$ ,  $\mu_{\text{eff}}$  is the effective viscosity,  $P$  the modified pressure obtained by subtracting hydrostatic pressure from local pressure,  $F_m$  the body forces in respective directions,  $\rho$  the density of the material,  $\delta_{mn}$  is Kronecker delta. The governing equation for quasi-steady state analysis with respect to moving coordinate system ( $x_1, x_2, x_3$ ) is expressed as

$$\rho \left( \mathbf{u}_n \frac{\partial \mathbf{u}_m}{\partial x_n} \right) = F_m + \frac{\partial}{\partial x_m} \left[ -P\delta_{mn} + \mu_{\text{eff}} \left( \frac{\partial \mathbf{u}_m}{\partial x_n} + \frac{\partial \mathbf{u}_n}{\partial x_m} \right) \right] - \rho V_w \frac{\partial \mathbf{u}_n}{\partial x_2} \quad (27)$$

Figure 1 describes various driving forces and corresponding boundary interactions during the heat transfer and fluid flow analysis. The body force in laser welding consists of buoyancy force only. The buoyancy force acts in  $x_3$  i.e. z-direction and is expressed considering Boussinesq approximation as (Reddy & Gartling, 2000)

$$F_3 = -\rho\beta(T - T_{\text{ref}})g \quad (28)$$

where  $\beta$  is the coefficient of thermal expansion,  $g$  the gravitational acceleration, and  $T_{\text{ref}}$  the reference temperature. The continuity equation (conservation of mass) for incompressible fluid is expressed as

$$\frac{\partial \mathbf{u}_m}{\partial x_m} = 0 \quad (29)$$

The energy equation of transient state is expressed as (Reddy & Gartling, 2000)

$$\frac{\partial}{\partial x_m} \left( k_{\text{eff}} \frac{\partial T}{\partial x_m} \right) + \dot{Q} = \rho C_p \left( \frac{\partial \mathbf{u}_n}{\partial t} + \mathbf{u}_n \frac{\partial T}{\partial x_m} \right) \quad (30)$$

where  $k_{\text{eff}}$  refer to effective thermal conductivity of liquid metal. The last term of the right hand side indicates the energy transport within the melt pool due to movement of liquid metal which was absent in conduction heat transfer analysis. The equation for the conservation of energy in pseudo-steady state is stated in 3D Cartesian coordinate system as

$$\frac{\partial}{\partial x_m} \left( k_{\text{eff}} \frac{\partial T}{\partial x_m} \right) = \rho C_p \left( \mathbf{u}_n \frac{\partial T}{\partial x_m} - V_w \frac{\partial T}{\partial x_2} \right) \quad (31)$$

The solution boundaries for both of mass and momentum equations are defined by the solid-liquid interface and the free surface of the weld pool which is assumed flat to avoid extra computational effort. A no-slip boundary condition for laminar flow at the solid-liquid interface is expressed as

$$\mathbf{u}_m = 0 \quad (32)$$

A slip boundary condition is expressed along the symmetric plane as

$$u_1 = 0, \quad \frac{\partial u_2}{\partial x_1} = 0 \quad \text{and} \quad \frac{\partial u_3}{\partial x_1} = 0 \quad (33)$$

The free surface of weld pool is subjected to surface tension force and the corresponding boundary conditions are expressed as

$$\mu \frac{\partial u_1}{\partial x_3} = f_L \frac{\partial \gamma}{\partial T} \frac{\partial T}{\partial x_1} \quad ; \quad \mu \frac{\partial u_2}{\partial x_3} = f_L \frac{\partial \gamma}{\partial T} \frac{\partial T}{\partial x_2} \quad ; \quad u_3 = 0 \quad (34)$$

where  $\gamma$  is the temperature dependent surface tension coefficient and  $f_L$  is the volume fraction of liquid metal along the weld pool top surface.

The penalty finite element method is designed in the present case to solve momentum equations by linking the continuity equation as constraint with the pressure and is expressed as

$$P = -\lambda \left( \frac{\partial \mathbf{u}_m}{\partial x_m} \right) \quad (35)$$

where  $\lambda$  is the penalty parameter that is set as equal to a large number so that it can satisfy the continuity equation (Reddy & Gartling, 2000). To avoid nonlinearity due to presence of velocity term in the convective term, the velocities ( $u_1^0, u_2^0, u_3^0$ ) are made independent from the nodal velocity variables. Hence,  $u_1^0, u_2^0$  and  $u_3^0$  for an element are calculated as average of the corresponding nodal velocity components. The velocity variable within the element is expressed

$$\mathbf{u}_m = \sum_{i=1}^8 [N_i] \{u_m^i\}; \quad \text{where } m = 1, 2, 3 \quad (36)$$

Equation (26) for a specific element 'e' can be written in a matrix form as

$$[M^e] \frac{\partial \{U\}}{\partial t} + \{ \bar{C}^e \} + [\hat{K}^e] + [K^e] \{U\} = \{F^e\} \quad (37)$$

where

$$[M^e] = \int_{\Omega^e} \rho N_i N_j d\Omega; \quad [\hat{K}_{mn}^e] = \int_{\Omega^e} \lambda \frac{\partial N_i}{\partial x_m} \frac{\partial N_j}{\partial x_n} d\Omega \quad (38, 39)$$

$$[K_{mn}^e] = \int_{\Omega^e} \mu \frac{\partial N_i}{\partial x_m} \frac{\partial N_j}{\partial x_n} d\Omega; \quad [\bar{C}^e] = \int_{\Omega^e} \rho \sum_{m=1}^3 \left( u_m^0 N_i \frac{\partial N_j}{\partial x_m} \right) d\Omega; \quad (40, 41)$$

$$\{F^e\} = \int_{\Omega^e} N_i \dot{F} d\Omega; \quad \{U\} = \{\{u_1^i\} \quad \{u_2^i\} \quad \{u_3^i\}\}^T \quad (42, 43)$$

$$i, j = 1, 2, 3, 4, 5, 6, 7, 8; \quad m, n = 1, 2, 3 \quad (44)$$

Similarly, eq. (27), in the case of quasi steady state analysis is expressed as

$$\{[M^e] + [\bar{C}^e] + [\hat{K}^e] + [K^e]\} \{U\} = \{F^e\} \quad (45)$$

where

$$[M^e] = - \int_{\Omega^e} \rho V_w N_i \frac{\partial N_j}{\partial x_2} d\Omega; \quad (46)$$

All other terms of eq. (45) are already defined. For all the elements in the solution domain, the assembly form of momentum equations for quasi-steady state analysis is further written as

$$[\bar{M}] \{U\} = \{F\} \quad (47)$$

where

$$[\bar{M}] = [M] + [\bar{C}] + [\hat{K}] + [K] \quad (48)$$

However, the integral term involving the penalty function i.e.  $[\hat{K}]$  matrix in the derivation of eq. (37) or (48), should be under-integrated (one point less) than the viscous and the convective terms i.e.  $[K]$  and  $[\bar{C}]$  matrices (Reddy & Gartling, 2000).

By similar mathematical treatment of momentum equations, the energy equation for quasi-steady state analysis can be represented in matrix form for any specific element 'e' as

$$[H^e] \{T\} + [C^e] \{T\} + [S^e] \{T\} + [\bar{H}^e] \{T\} = \{f_o^e\} + \{f_q^e\} + \{f_h^e\} \quad (49)$$

where

$$[C^e] = \int_{\Omega^e} \rho C_p \sum_{m=1}^3 \left( u_m^0 N_i \frac{\partial N_j}{\partial x_m} \right) d\Omega \quad (50)$$

All other terms of energy equation are already defined in conduction heat transfer analysis. The matrix equation of transient energy equation follows similar procedure described above.

The presence of surface active elements such as sulfur and oxygen play an important role in the formation weld pool geometry since the surface tension fore (i.e. surface tension coefficient) differs considerably in molten material which is a function of weight percent of

surface active elements and temperature. The detailed variation of surface tension gradient as a function of temperature and activity of solute is represented as (Sahoo et al., 1988)

$$\partial\gamma/\partial T = -A - R_g \Gamma_s \ln(1 + C_s b_i) - \frac{C_s b_i}{1 + C_s b_i} \frac{\Gamma_s \Delta H^\circ}{T} \quad (51)$$

where  $\partial\gamma/\partial T$ ,  $A$ ,  $\Gamma_s$ ,  $C_s$ ,  $b_i$ ,  $\Delta H^\circ$  and  $R_g$  referred to the surface tension gradient, adsorption coefficient, surface excess at saturation, segregation coefficient, activity of the 'i<sup>th</sup>' species, heat of adsorption and characteristic gas constant respectively. Their computed results showed that the surface tension decreased linearly with temperature when the sulfur content in the weld pool was negligible. At a constant temperature the surface tension showed an upward curvature with increase in sulfur content. When the sulfur content in the weld pool was significant, surface tension first increased and then decreased with the increase in temperature as surface active elements tended to segregate at higher temperature. Present numerical model of heat transfer and fluid considers the formation of weld geometry due to the effect of surface active element present in the parent material.

### 3. Inverse modelling approach

The reliability of numerical model intuitively depends on correct representation of several input parameters that is essential in modelling calculations. A number of inverse methods have recently been used in conjunction with numerical models for determining suitable values of required uncertain model parameters (De & DebRoy, 2005; Mishra & DebRoy, 2005; Bag & De, 2008; Bag et al., 2009; Bag & De, 2010). This is achieved in the present work by integrating a real number based differential evolution (DE) algorithm for the numerical models. The link between the numerical model and optimization algorithm as well as search direction towards the optimum conditions are evaluated through the formation of a suitable objective function which is defined as

$$O(\theta) = \sum_{l=1}^M \left[ \frac{w_l^c - w_l^{\text{exp}}}{w_l^{\text{exp}}} \right]^2 + \left[ \frac{p_l^c - p_l^{\text{exp}}}{p_l^{\text{exp}}} \right]^2 = \sum_{l=1}^M [w_l^* - 1]^2 + [p_l^* - 1]^2 \quad (52)$$

where 'c' refers to computed value from numerical model, 'exp' refers to experimentally measured values and '\*' refers to non-dimensional form of the variables that indicate the extent of over or under-prediction of variables. The subscript l refers to specific data points in a series of M number of total data points. In equation (52),  $\theta$  stands for the independent variable set which is unknown. The objective function,  $O(\theta)$ , depicts the error between the estimated from numerical model and the corresponding measured values with similar process conditions with M number of observations. However, it is pointed out that this integrated modelling calculation considers few experimental results. Differential evolution (DE), proposed by Storn (Storn, 1997), is a derivative of genetic algorithm (GA). The algorithm is described elsewhere (Price et al., 2005).

Figure 4 describes the overall solution algorithm of the integrated model. The algorithm starts with the creation of large volume of discrete data sets that referred to as population. Each individual in this population is a possible solution and consists of assumed values of

the uncertain parameters, to begin with. The numerical solutions are carried out using all the individuals and the corresponding error in prediction ( $O(\theta)$ ) for each individual is computed. In case the minimum value of the error is beyond a pre-defined value of tolerance in prediction, further iteration or calculations are discouraged. The choice of the best solution is dictated by the numerical value of objective function after N iterations.

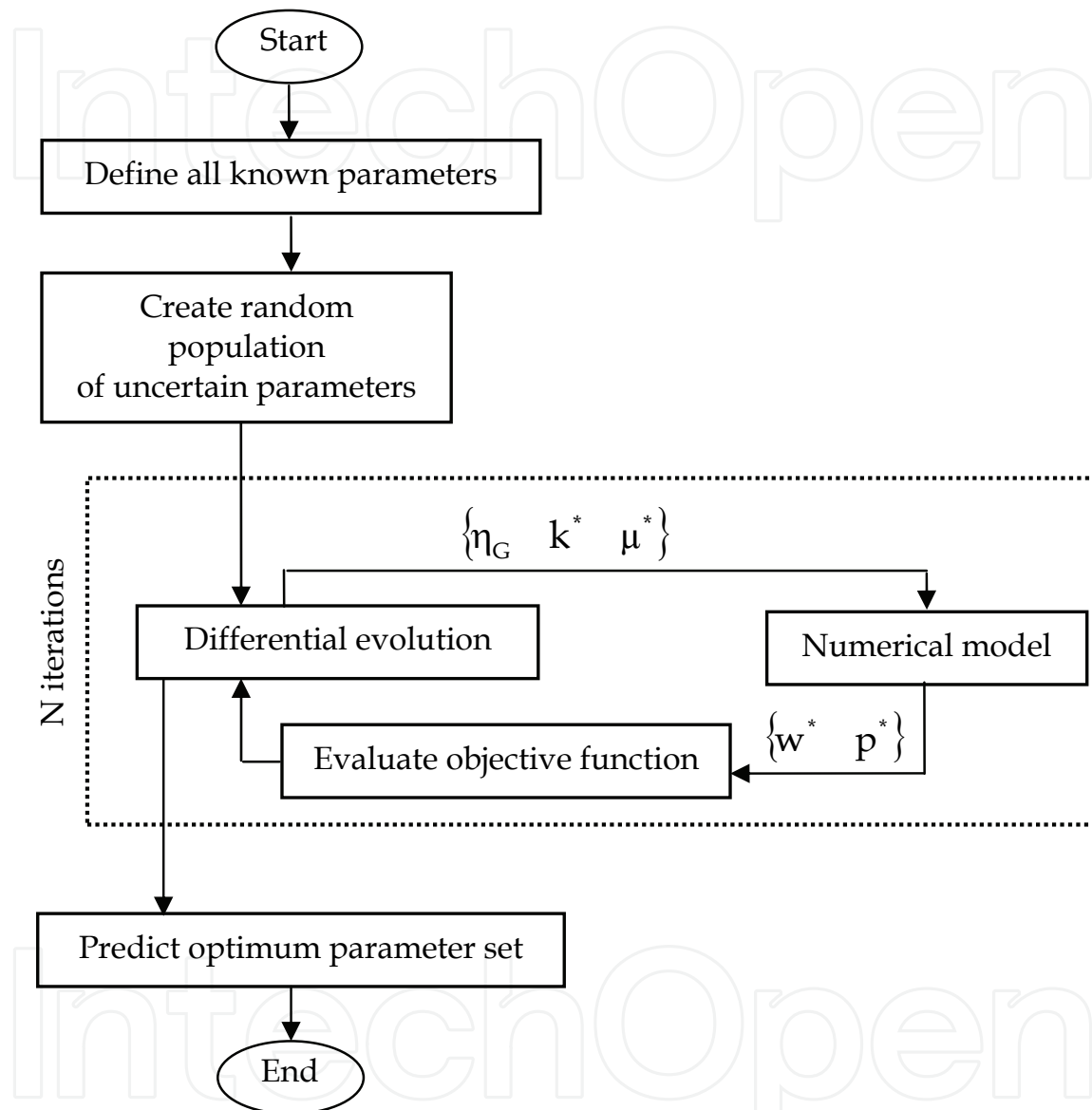


Fig. 4. Overall solution algorithm of integrated model.

#### 4. Results and discussions

The overall results of the model calculations are arranged in the following sequence. First, the identification of uncertain parameters is done through inverse modelling approach. A detail sensitivity analysis of these parameters on weld geometry is performed to get the range of physically meaningful values and to identify less or more sensitive parameters related to the process modelling. Next, the comparison between experimental and

numerically calculated weld geometry are described in various process conditions using the optimized set of uncertain parameters. The influence of surface active elements on the shape of weld pool geometry is highlighted here. The relative importance of various driving forces during momentum transport within weld pool is performed next. Finally, the numerically computed weld geometry is compared using conduction only heat transfer and transport phenomena based heat transfer and fluid flow analysis.

To validate the numerical model, several laser weld experiments are conducted both for spot and linear welding using pulsed Nd:YAG laser. In addition to that some of the experimental results are considered from independent literature (Pitscheneder et al., 1996; Tzeng, 2000). The experiments are conducted at two cases: one for spot welding at average laser power 1.0 kW at several on-times varying from 0.5 to 2.5 s and another for linear welding at average power of 1.2 kW at travel speed varying from 5 to 10 mm/s with different weight percent of sulfur present in low carbon steel. The effective beam radius of the incident laser beam is measured as 1.20 mm for all the experimental conditions. The weld samples are prepared on 2.0 mm thick low carbon steel sheet. The chemical composition of the material is described elsewhere (Frewin & Scott, 1999). Table 1 describes the various welding conditions (six cases) and corresponding parameters used to conduct experiments. Figure 5 depicts the measured weld dimensions corresponding to all six cases used to validate the numerically computed results.

a, b considered from literature

Case	Type of welding	Material	Sulfur content (wt %)	Laser power (kW)	Effective beam radius (mm)	Power density (kW/mm <sup>2</sup> )	Laser on-time (s) /travel speed (mm/s)
i	Spot welding	High-speed steel <sup>a</sup>	0.002	5.2	1.4	845	0.1 ~ 0.75
ii			0.015				
iii		Low carbon steel	0.002	1.0	0.6	885	
iv	Linear welding	Bare steel <sup>b</sup>	0.010	0.4	0.4	796	6 ~ 8
v		Low carbon steel	0.002	1.2	0.6	1062	5 ~ 10
vi			0.012				5 ~ 7

Table 1. Experimental conditions of laser welding used in present work.

It is evident from Fig. 5(a) that with the increase of laser on-time the weld pool dimensions increases since it absorbs more energy at higher weld time. On the other hand, the weld dimensions decreases with increase in travel speed (Fig. 5(b)) since the heat input per unit length decreases with increase in travel speed. However, it is also observed from Fig. 5 that the weld pool aspect ratio (penetration to width) varies from 0.14 ~ 0.60 and the power density varies from 796 to 1062 W/mm<sup>2</sup>, which indicates typical weld pool shapes in conduction mode laser welding process. The weld dimensions differ considerably between

case-i and case-ii, and between case-v and case-vi irrespective of similar experimental conditions except the weight percent of sulfur content in the parent material. This manifests the predominance effect of convective heat transfer in weld pool in the presence of considerable amount of surface active elements. Table 2 describes the material properties used in present numerical calculation and to calculate various non-dimensional numbers.

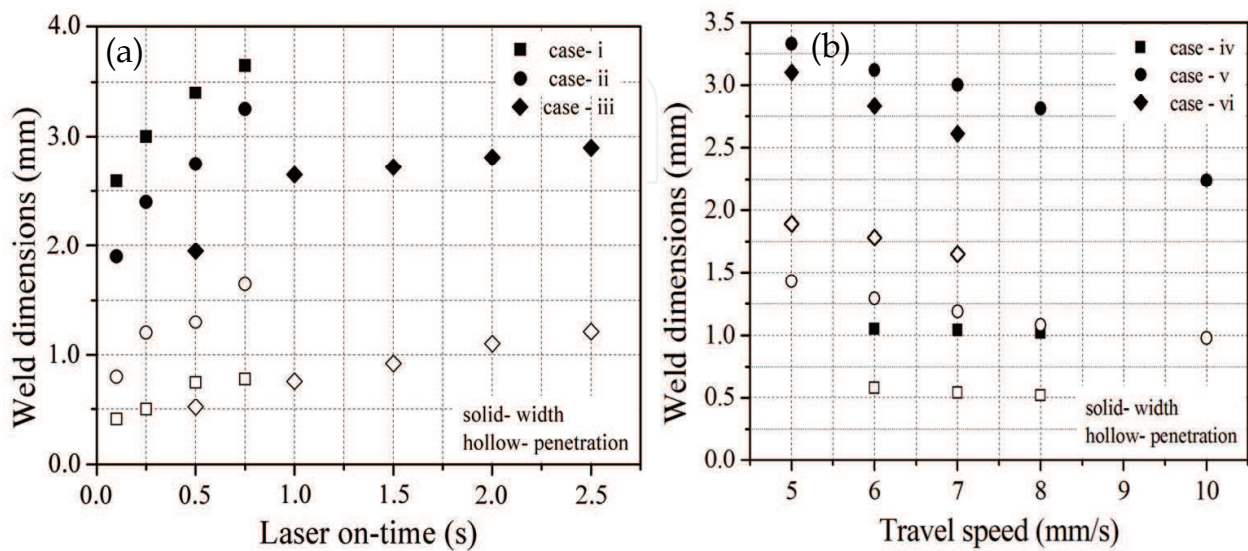


Fig. 5. Experimentally measured weld pool dimensions for (a) laser spot welding and (b) linear welding.

#### 4.1 Identification of uncertain parameters

It is evident from theoretical formulation of finite element based numerical model that it involves various uncertain parameters such as absorption coefficients ( $\eta_G, \eta_V$ ), distribution coefficient ( $d_i$ ), effective radius of laser beam ( $r_{eff}$ ), coefficient of uneven heat distribution in linear welding ( $f$ ) and material properties at high temperature ( $k_{eff}, \mu_{eff}$ ). Hence, a detailed sensitivity analysis of the computed weld dimensions on these uncertain parameters is performed by using 3D numerical model at various welding conditions. It is observed that with the increase of absorption coefficients, the weld pool dimensions increase with the weld penetration being more sensitive than weld width. This is primarily due to smaller thickness dimension in comparison to the length and width of the plate. An increase in the value of effective thermal conductivity and viscosity reduces weld width and increases weld penetration. Higher values of thermal conductivity reduce the surface temperature gradient and hence the convective transport of heat towards the periphery that reduces weld width. Greater values of effective viscosity also reduce the convective transport of heat leading to the smaller weld width. A secondary sensitivity analysis of weld dimensions is also performed on  $d_i$  and  $f$ . It is realised that these parameters have negligible influence over a wide range of changes in the process parameters. Hence these are considered as known parameters to make the inverse approach tractable with the minimum number of uncertain parameters. The effective radius of laser beam is considered as certain parameter. The uncertain parameter sets of conduction heat transfer analysis and transport phenomena based heat transfer and fluid flow analysis are considered as

$$\{\theta^{\text{cond}}\} = \{\eta_G \quad \eta_v\} \quad (53a)$$

$$\{\theta^{\text{conv}}\} = \{\eta_G \quad k_{\text{eff}}/k_s \quad \mu_{\text{eff}}/\mu\} \equiv \{\eta_G \quad k^* \quad \mu^*\} \quad (53b)$$

where  $k^*$  and  $\mu^*$  is non dimensional form with respect to  $k_s$  (conductivity at room temperature) and  $\mu$  (molecular value at room temperature), respectively.

Parameters	Value	
	Low carbon steel	Bare steel
Density ( $\rho$ ) - kg m <sup>-3</sup>	7.8 x 10 <sup>3</sup>	8.0 x 10 <sup>3</sup>
Melting temperature ( $T_m$ ) - K	1790	1800
Specific heat ( $C_p$ ) - J kg <sup>-1</sup>	755.0	745.8
Latent heat (L) - J kg <sup>-1</sup> K <sup>-1</sup>	2.45 x 10 <sup>5</sup>	2.50 x 10 <sup>5</sup>
Thermal conductivity ( $k_s$ ) - J s <sup>-1</sup> m <sup>-1</sup> K <sup>-1</sup>	32.4	31.2
Coefficient of thermal expansion ( $\beta$ ) - K <sup>-1</sup>	2.0 x 10 <sup>-5</sup>	2.0 x 10 <sup>-5</sup>
Temperature coefficient of surface tension ( $\frac{d\gamma}{dT}$ ) of pure iron - N m <sup>-1</sup> K <sup>-1</sup>	-0.5 x 10 <sup>-3</sup>	-0.5 x 10 <sup>-3</sup>
Molecular viscosity ( $\mu$ ) - kg m <sup>-1</sup> s <sup>-1</sup>	6.0 x 10 <sup>-3</sup>	6.0 x 10 <sup>-3</sup>

Table 2. Material properties used in numerical calculation.

To start with the optimization calculation, the feasible ranges of uncertain parameters are defined first. A correct choice of the parameter ranges also influence the overall computational time. Table 3 reports the feasible range of parameters used for optimization calculation and the optimum values of uncertain parameters derived from the integrated model. However, the choice of the initial range of parameters is based on literature reported results (Benyounis et al., 2005; Liu et al., 1993; Tzeng, 1999; Tanriver et al. 2000) as well as the experience gained from several numerical experiments. It is to be noted that the parameters for case- i and case - ii are considered from independent literature (Pitscheneder et al., 1996) without performing any optimization calculation. Moreover, the estimation of the optimum parameters is independent of the presence of surface active elements i.e. the optimum uncertain parameter set is similar for a laser process irrespective of the surface active elements presents in the material. Table 4 describes the typical values of the objective function and the corresponding uncertain parameter set after 23 iterations for case - iii. Further improvement in the value of the objective function was not possible corresponding to predefine values of control parameters (crossover constant, mutation factor and number



of initial population) of DE. The optimum set of parameter is chosen from table 4 corresponding to the minimum value of objective function.

Type of welding	Mode of analysis	Uncertain parameter	Range of parameter	Optimum parameter
Spot welding (case - iii)	Conduction heat transfer	$\eta_G$	0.20 ~ 0.50	0.37
		$\eta_V$	0.20 ~ 0.70	0.48
	Heat transfer and fluid flow	$\eta_G$	0.20 ~ 0.50	0.36
		$k^*$	1.0 ~ 10.0	5.2
		$\mu^*$	1.0 ~ 10.0	4.5
Linear welding (case -iv, v, vi)	Conduction heat transfer	$\eta_G$	0.20 ~ 0.50	0.36
		$\eta_V$	0.20 ~ 0.70	0.51
	Heat transfer and fluid flow	$\eta_G$	0.20 ~ 0.50	0.38
		$k^*$	1.0 ~ 10.0	6.0
		$\mu^*$	1.0 ~ 10.0	7.0

Table 3. Optimum calculation of uncertain parameters by selecting range of parameters.

Individual index	$O(\theta^{conv}) \times 10^{-3}$	$\eta_G$	$k^*$	$\mu^*$
1	4.2	0.385	5.01	4.81
2	3.6	0.391	5.42	4.53
3	4.7	0.392	5.32	5.02
4	1.7	0.382	5.21	4.53
5	2.3	0.374	5.91	4.66
6	2.2	0.365	5.65	4.12
7	3.9	0.331	5.78	4.44
8	<b>1.2</b>	<b>0.381</b>	<b>5.22</b>	<b>4.51</b>
9	2.6	0.394	5.10	4.78

Table 4. Optimum set of uncertain parameters in laser spot welding using DE corresponding to case - iii using only three experimental data sets.

#### 4.2 Prediction of weld geometry

Figure 6 describes the comparative study for the prediction of a target weld pool dimensions using three different heat source models: surface heat flux without any volumetric heat source, volumetric heat source with predefined heat source term and adaptive volumetric heat source. It is evident from the figure that surface only heat flux is not always satisfactory to predict the weld dimensions whereas volumetric heat source models are more reliable to such prediction. Volumetric heat with predefined heat source terms predicts the target weld dimensions with a-priori knowledge of weld dimensions. However, adaptively defined volumetric heat source predicts target weld geometry without the knowledge of target weld dimensions since the growth of source terms evolves with time as weld pool grows. Hence,

the adaptive nature of volumetric heat source term essentially enhances the robustness and applicability of conduction mode laser welding process.

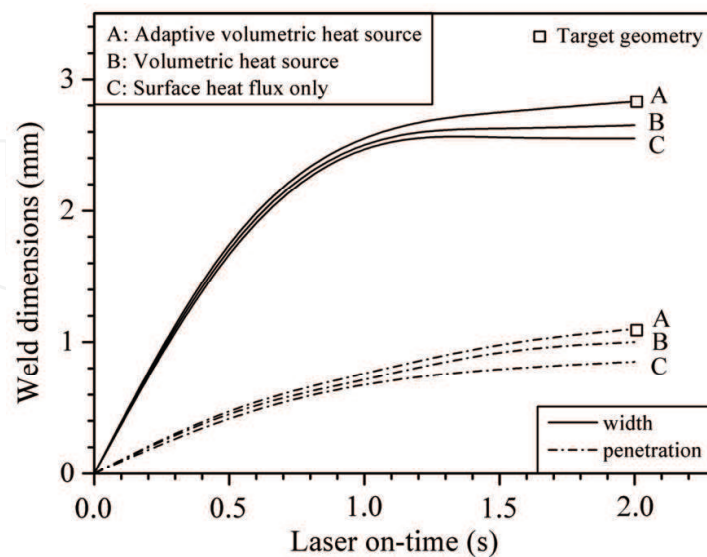


Fig. 6. Prediction of weld dimensions using various heat source models.

The experimentally measured weld dimensions for laser welding process is used to compare the numerically computed results using the optimum set of uncertain parameters of heat transfer and fluid flow analysis. Figure 7 describes such comparison both for spot and linear welding. The relative error in this case is defined by

$$w_R = \left| \frac{w^c - w^{\text{exp}}}{w^{\text{exp}}} \right|; \quad p_R = \left| \frac{p^c - p^{\text{exp}}}{p^{\text{exp}}} \right| \quad (54)$$

where  $w_R$  or  $p_R$  represents the deviation of the calculated dimensions with reference to the corresponding experimental values. It is evident from Fig. 7(a) that the relative errors for most of the cases are smaller than 0.10. However, the transport phenomena based heat transfer and fluid flow model is more proficient for relatively bigger weld pool (higher on-time) for all the three cases. It is evident from Fig. 7(a) that the relative error for low laser on-time (case - i and case - iii) is high and this is possibly due to the lack of reaching the fully developed flow. In this case the conduction heat transfer model may be appropriate to predict weld dimensions. Figure 7(b) depicts the relative errors for linear welding for three cases. It is evident from this figure that the relative errors are high for comparatively smaller weld dimensions. However, the overall relative error is below 0.07. This indicates that the numerical model is robust enough to predict weld dimensions over a range of variable process parameters (travel speed = 5 ~ 10 mm/s, sulfur content = 0.002 ~ 0.012 wt %).

Figure 8 describes the 3D computed temperature and velocity profile for laser spot and linear welding corresponding to laser on-time of 1.0 s (case - iii of Table 1) and travel speed 10 mm/s (case - v of Table 1), respectively. The temperature and velocity profile for spot welding is symmetric with respect to XZ plane (Fig. 8a). Since the surface tension coefficient is negative (for low sulfur content), the material moves from centre of laser beam towards

the periphery and the buoyancy force acts in upward direction (Z direction). The combined effect of these two driving forces makes circulation loop in clockwise direction.

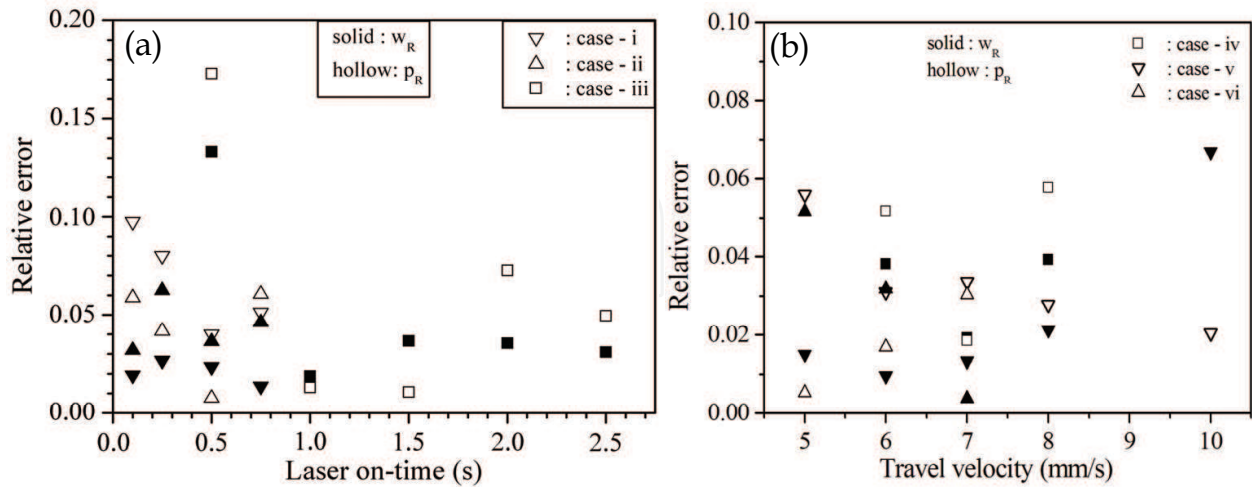


Fig. 7. Comparison between computed and experimentally measured weld dimensions in case of (a) spot welding and (b) linear welding.

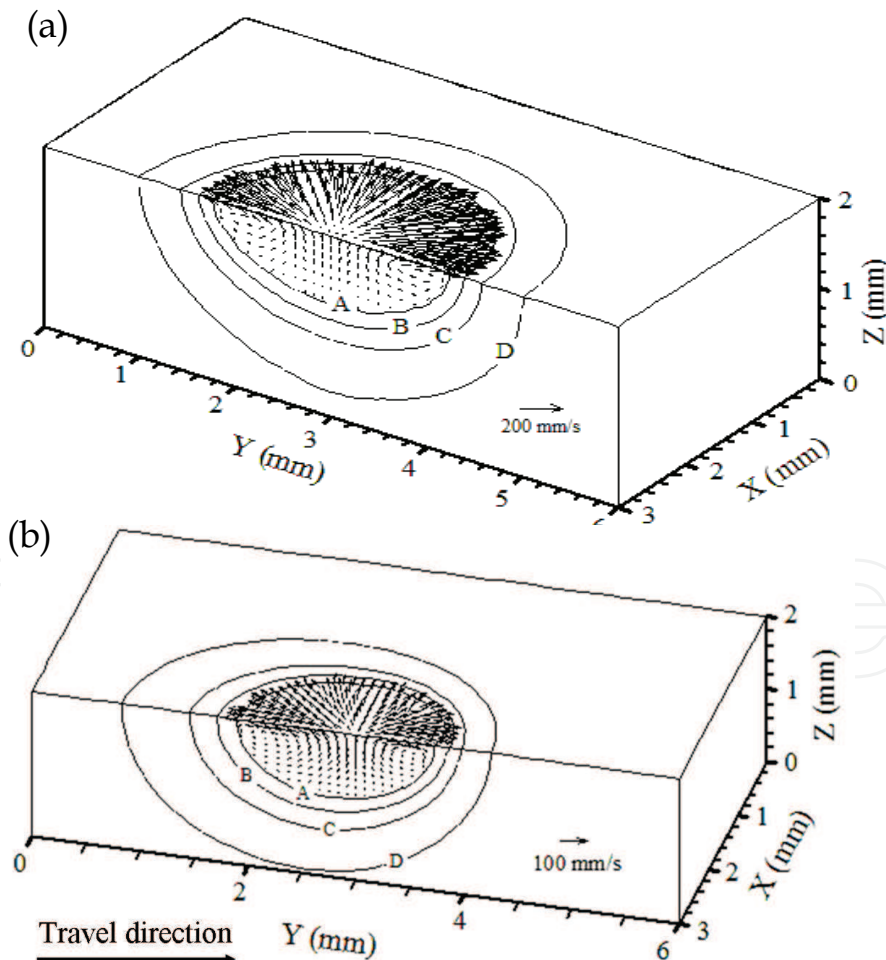


Fig. 8. A 3D computational view of temperature and velocity distribution in (a) spot welding and (b) linear welding (A - 1780 K, B - 1473 K, C - 1203 K, D - 993 K).

This nature of material movement in weld pool enhances weld width and decreases the weld penetration. Similar nature of material movement is also observed in the case of linear welding (Fig. 8b). However, in this case the temperature and velocity distribution is asymmetric due to the linear weld velocity along Y-direction. Figure 9 depicts the comparison between the experimentally measured macrograph (left side) with the computed weld geometry (right side) corresponding to travel speed of 7 mm/s for case - v. The cross-section of computed weld geometry is extracted from XZ plane on the location of the centre of laser beam. A good agreement of the shape and size of computed weld pool with the corresponding experimentally measured result is observed in Fig. 9.

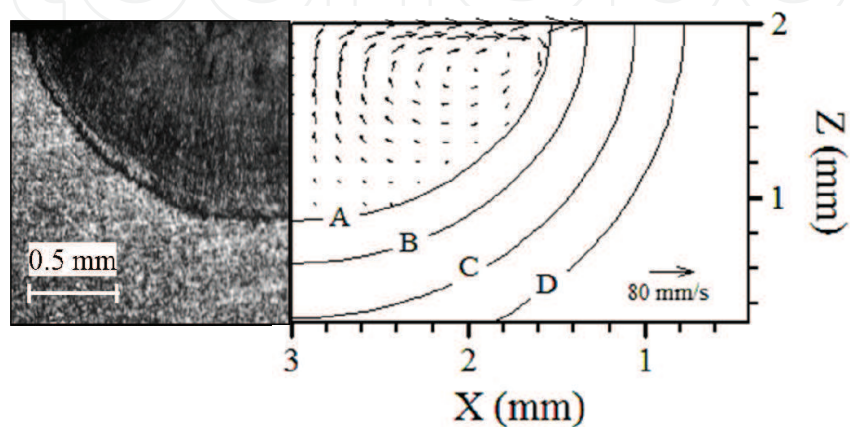


Fig. 9. Comparison between computed and experimentally measured weld macrograph (A - 1780 K, B - 1473 K, C - 1203 K, D - 993 K).

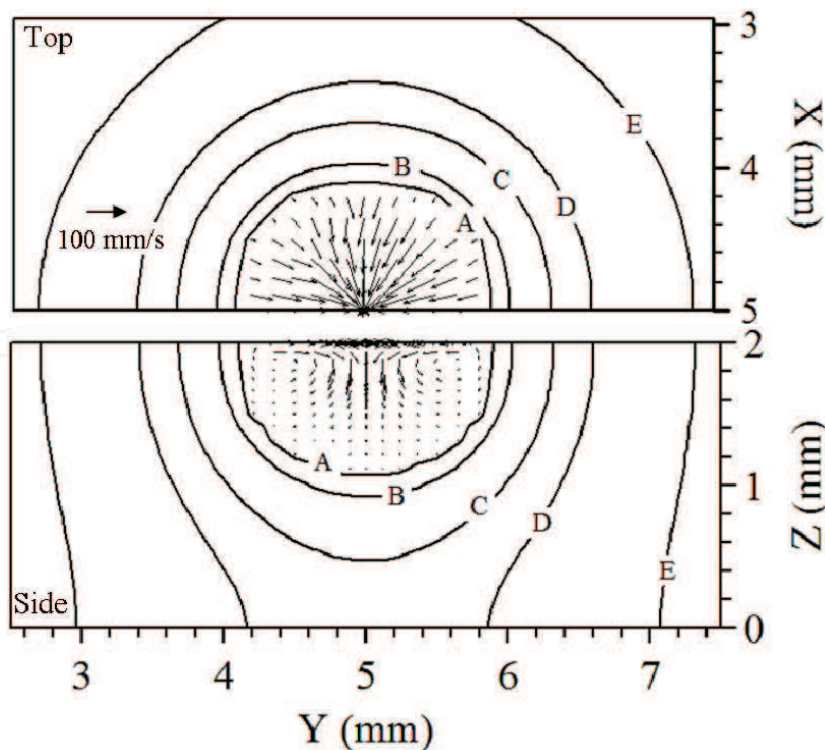


Fig. 10. Distribution of temperature and velocity profile in laser spot welding at on-time 0.1 s for case - ii (A - 1620 K, B - 1500 K, C - 1200 K, D - 1000 K, E - 773 K).

Figure 10 shows the nature of fluid flow in laser spot welding for the material having 0.015 weight percent of sulfur. It is evident from the figure that the liquid metal flows from periphery to the centre of heat source. This nature of flow is due to the positive surface tension coefficient at this high percentage of surface active elements present in molten material. It is also obvious that the reversal nature of flow reduces the weld width and increases the penetration as compared to molten material having small percentage of sulfur for similar welding conditions. This trend is also observed in experimental results.

Figure 11 describes the shape of weld geometry in similar welding conditions and material except having different quantities of sulfur. The resultant velocity direction is completely opposite in these two cases. This clearly indicates the importance of the coupled heat transfer and fluid flow simulation for the prediction of weld pool geometry in the presence of surface active elements within parent material. To achieve similar trend with single set of uncertain parameters is nearly impossible for conduction heat transfer analysis alone.

### 4.3 Relative importance of driving forces

The validation of numerical heat transfer and fluid flow model in fusion welding process is extremely difficult or nearly impossible by means of experiments (Pitscheneder et al., 1997). Hence, a relatively simple approach is followed by researchers (Bag et al., 2009; Oreper & Szekely, 1987; Hong et al., 2003; Zhang et al., 2003; He et al., 2003; He et al., 2005). The relative importance of driving forces for liquid metal motion is quantitatively analyzed using dimensionless numbers and an order of magnitude analysis is followed to estimate the expected velocity of liquid metal (Bag et al., 2009). A comparison of the quantitative values obtained from the order of magnitude analysis and the numerical model stands to validate the fluid flow analysis in fusion welding process.

The relative importance of the mode of heat transfer within weld pool is evaluated by using Peclet number (Pe) which is defined by (He et al., 2003)

$$Pe = \frac{U_{av} \rho C_p L_{av}}{k_{eff}} \quad (55)$$

where  $U_{av}$  and  $L_{av}$  are the average velocity and average length on the top of weld pool surface. It is evident from eq. (48) that the liquid metal convection affects the heat transfer when Pe is large whereas small Pe indicates the heat dissipation mainly by conduction. Hence, the fluid flow analysis of molten weld pool is significant when Pe is more than one or well above one. Table 5 describes the computed values of Peclet number for various welding conditions (case - iii and case - v). It is evident from the quantitative values of Peclet number that convection within weld pool is significant as compared to only conduction analysis. Hence the transport phenomena based heat transfer analysis is necessary to predict weld dimensions for these welding conditions.

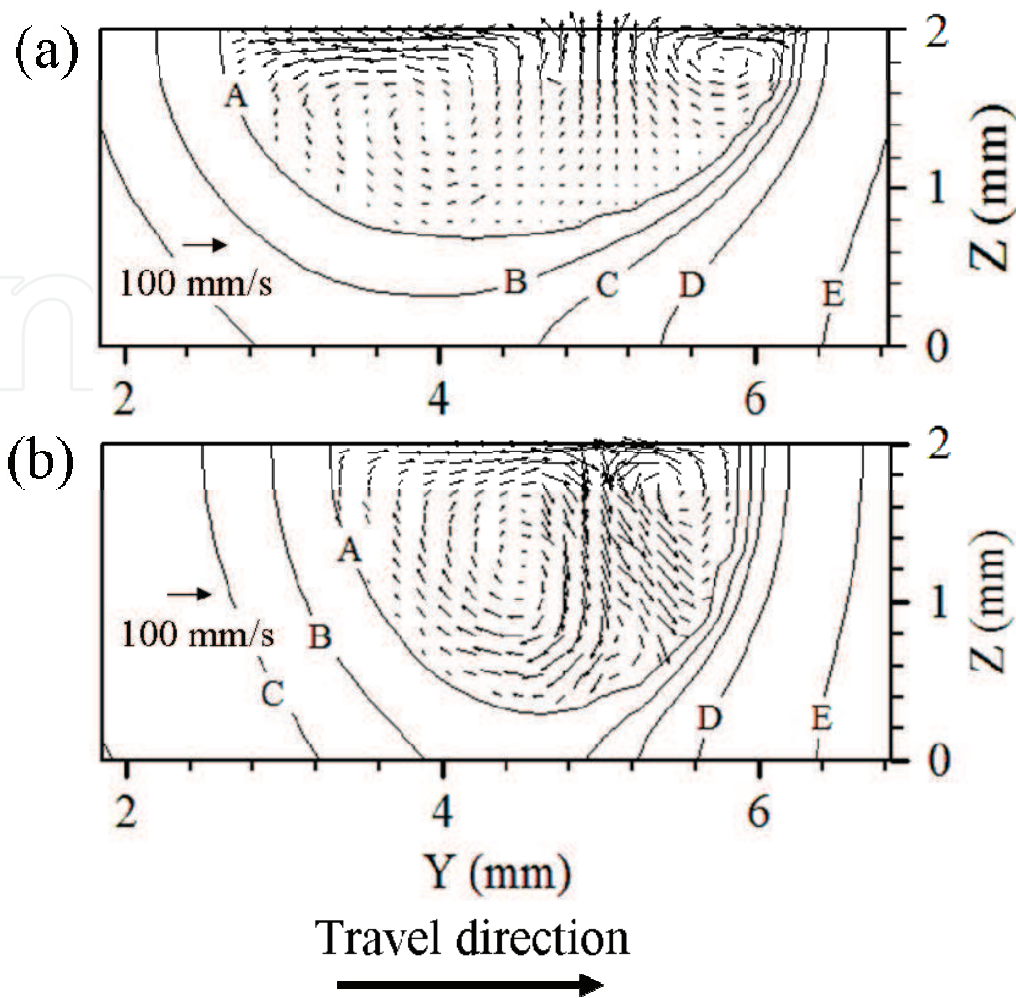


Fig. 11. Distribution of temperature and velocity profile in linear laser welding at travel speed of 6 mm/s with different sulfur content in steel: (a) 0.002 wt % sulfur and (b) 0.012 wt % sulfur (A - 1780 K, B - 1473 K, C - 1203 K, D - 993 K, E - 773 K).

The transport phenomena in laser welding is characterised by three driving forces such as surface tension force, buoyancy force and viscous force. The relative importance of surface tension force is described by surface tension Reynolds number ( $R_{ST}$ ) which is the ratio of surface tension gradient force to viscous force, and is expressed as (He et al., 2005)

$$R_{ST} = \frac{\rho L_{av} \Delta T \left| \frac{\partial \gamma}{\partial T} \right|}{\mu_{eff}^2} \quad (56)$$

where  $\frac{\partial \gamma}{\partial T}$  the temperature coefficient of surface tension and  $\Delta T$  is the mean temperature difference between peak pool temperature and solidus temperature on the top of weld pool. The Grashof number (He et al., 2003) is defined by the ratio of buoyancy force to viscous force and is represented as

$$Gr = \frac{g\beta L_{CR}^3 \Delta T \rho^2}{\mu_{eff}^2} \quad (57)$$

where  $g$  is gravitational acceleration,  $\beta$  is the thermal expansion coefficient, and  $L_{CR}$  is the characteristics length. To understand the relative importance between surface tension force and buoyancy force, the dimensionless number is defined by the ratio of surface tension Reynolds number and Grashof number and is expressed as

$$R_{ST/B} = \frac{R_{ST}}{Gr} \quad (58)$$

From the order of magnitude analysis, the maximum velocity under surface tension force,  $U_{ST}$ , can be done assuming a boundary layer develops due to Marangoni shear stress and the maximum velocity occurs at a location approximately halfway between the heat source and weld pool edge (DebRoy & David, 1995),

$$U_{ST}^{3/2} \approx \left| \frac{\partial \gamma}{\partial T} \right| \left| \frac{dT}{dx} \right|_{x=w/4} \frac{w^{1/2}}{0.664 \rho^{1/2} \mu_{eff}^{1/2}} \quad (59)$$

where  $\frac{dT}{dx}$  is average temperature gradient on the top of weld pool at the position of  $w/4$ .

An order of magnitude analysis of the maximum velocity due to buoyancy driven flow is estimated as (He et al., 2003)

$$u_g = \sqrt{g\beta\Delta T p} \quad (60)$$

where  $p$  is the depth of weld pool.

The quantitative estimation of various dimensionless numbers for present welding conditions is reported in Table 5 by using material data depicted in Table 2. It is obvious from the tabulated data of  $R_{ST}$  that the viscous force is less significant as compared to surface tension force. However, the computed values of  $Gr$  indicate that viscous force is more significant as compared to buoyancy force. Overall, the analysis on the quantitative values of all driving force within molten pool indicates that surface tension force acts as the main driving force for the liquid metal movement in laser welding process. Hence the maximum magnitude of velocity is observed on the top of the weld pool (Fig. 8) due to the surface tension force. Figure 12 describes the comparison of maximum magnitude of expected velocity between order of magnitude analyses and predicted from numerical model. The relatively small deviation between these values indicates that the numerical model predicts the velocity distribution well.

Type of welding	On-time (s)/Travel speed (mm/s)	Dimensionless numbers			
		Pe	$R_{ST} (x10^3)$	$Gr (x10^{-2})$	$R_{ST/B} (x10^4)$
Spot welding (case - iii)	0.5	3.04	0.36	0.20	18.0
	1.0	6.41	1.1	1.20	9.5
	1.5	7.67	1.4	1.60	9.0
	2.0	8.30	1.6	1.90	8.5
	2.5	10.5	2.3	2.90	8.0
Linear welding (case - v)	5	9.91	0.14	2.20	6.0
	6	8.71	0.11	1.60	6.9
	7	7.59	9.10	1.20	7.4
	8	6.20	6.70	0.79	8.5
	10	5.03	4.90	0.37	13.0

Table 5. Quantative estimation of dimensionless numbers in fluid flow analysis of laser welding.

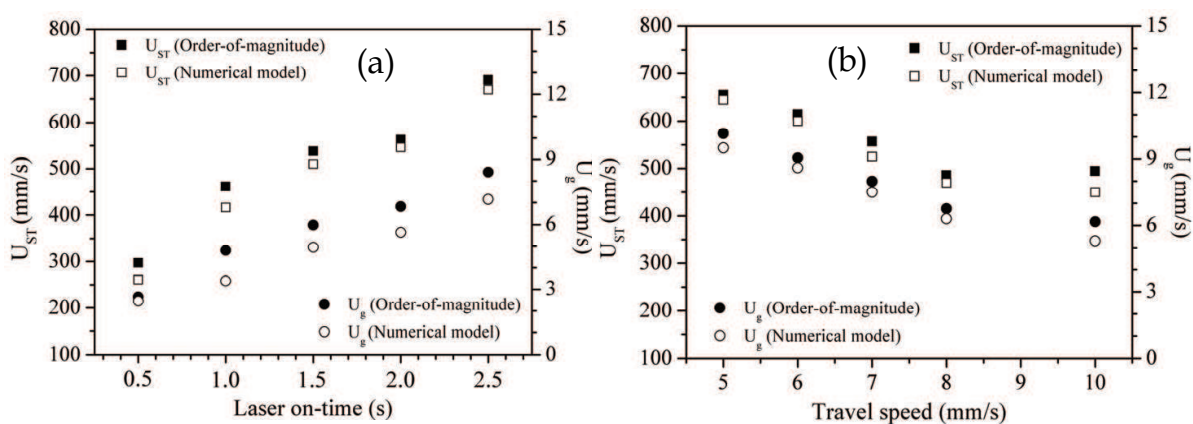


Fig. 12 Comparison of maximum magnitude of velocity between numerical model results and calculated from order of magnitude analysis in case of (a) spot welding (case - iii) and (b) linear welding (case - v).

#### 4.4 Comparative study between conduction and transport phenomena based model

Figure 13 describes the comparison between computed weld dimensions using both conduction heat transfer and transport phenomena based model in laser spot welding. This comparison is also performed with reference to experimentally measured results for similar welding conditions. It is obvious from Fig. 13(a) that the conduction model predicts weld geometry well in case of small geometry (low on-time) and material having low weight percent of sulfur whereas the transport phenomena based heat transfer and fluid flow model predicts bigger weld pool (high on-time) better. However, the conduction based model fails to predict the weld geometry for the material having considerable amount of surface active elements (0.015 wt % of sulfur). Figure 13(b) indicates that both the models predict weld geometry well since the surface active elements is less in this case (0.002 wt % sulfur). However, the transport phenomena based model predicts weld penetration well as compared to the conduction based model. Hence, it is concluded that the transport



phenomena based model is suitable for wide range of process capability i.e. longer laser on-time and presence of surface active elements. Figure 14 depicts a comparative study of weld dimensions in linear welding between conduction and convection based model with reference to experimentally measured results. It is obvious from Fig. 14 (a) that the convection based model predicts better than conduction based model results. This possibly due to fact that the material contains 0.010 weight percent of sulfur that changes the shape of weld geometry considerably as compared to material having low sulfur (0.002 wt %).

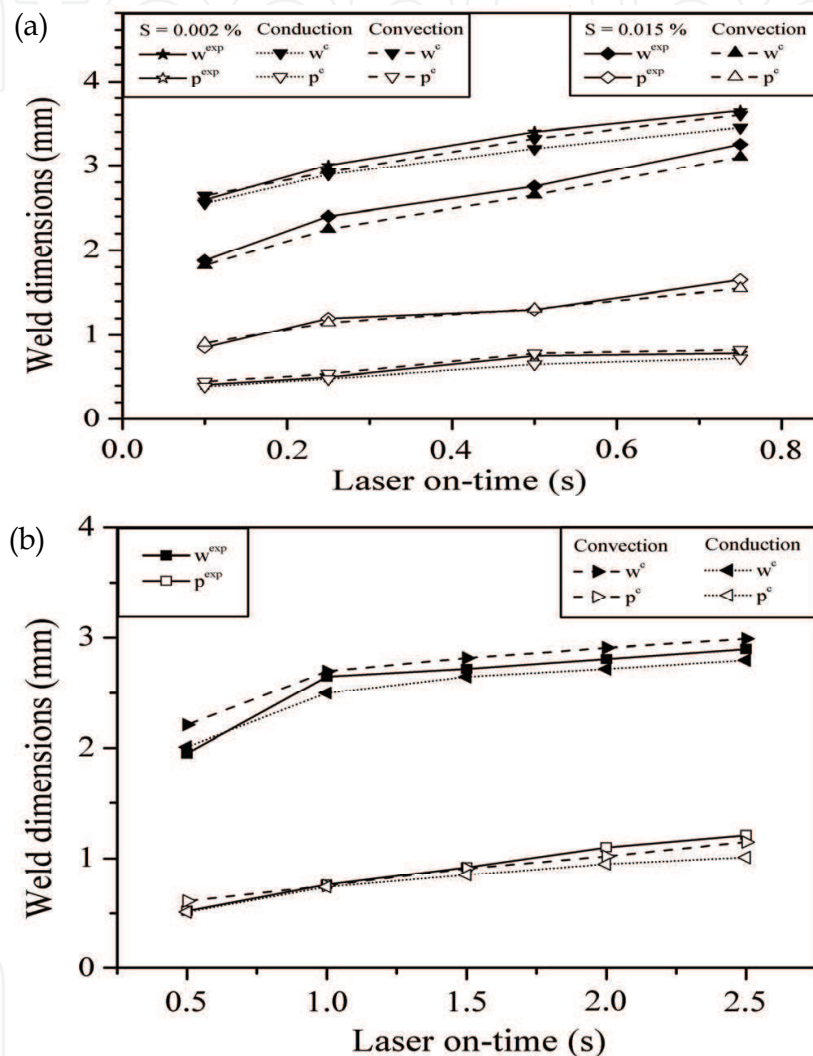


Fig. 13. Comparison of weld geometry prediction between conduction model and transport phenomena based heat transfer and fluid flow model in spot welding: (a) case - i and case - ii) and (b) case - iii.

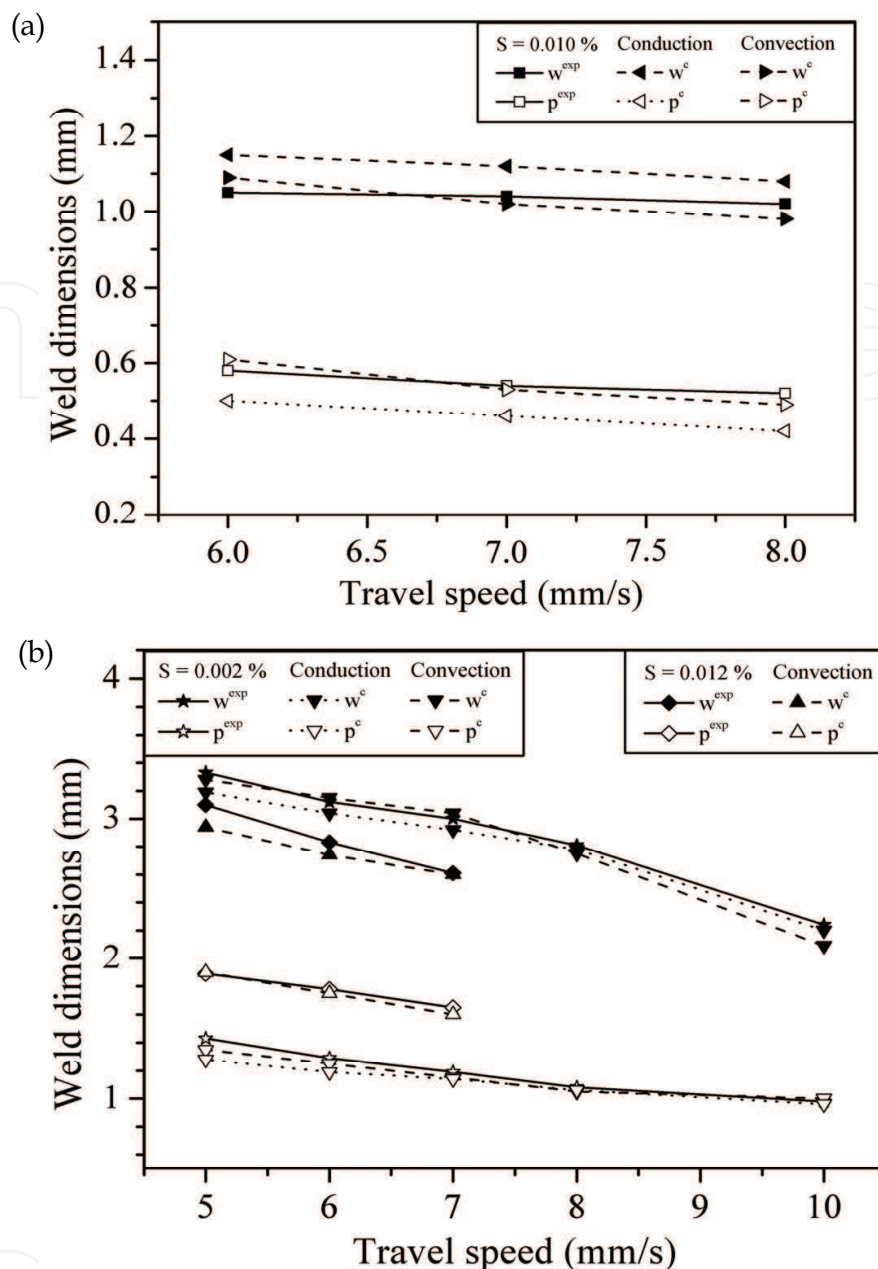


Fig. 14. Comparison of weld geometry prediction between conduction model and transport phenomena based heat transfer and fluid flow model in linear welding: (a) case - iv and (b) case - v and case vi.

## 5. Conclusions

An integrated model of conduction mode laser welding process is depicted in present work that is capable of undertaking 3D transient and pseudo-steady state heat conduction as well as transport phenomena based heat transfer and fluid flow analysis in weld pool using finite element method. The real parameter based differential evolution (DE) assists the numerical process model to predict uncertain parameters in an inverse manner. Conduction heat transfer based numerical models are important when weld geometry is small and, fast and repetitive calculation is of primary interest. The proposed adaptively defined volumetric

heat source term in the frame of conduction heat transfer analysis is successfully demonstrated for a number of laser spot and linear welds. Transport phenomena based heat transfer and fluid flow analysis enhances the reliability of computed temperature field of comparatively bigger weld pool and is essential for material having considerable amount of surface active elements. The quantitative estimation of the fluid velocity is validated through order of magnitude analysis. The significant quantitative knowledge extracted from this work in laser welding is expected to improve the physical understanding of laser welding process and serve as a basis for the design of welding process.

## 6. References

- Bag, S. & De, A. (2008). Development of a three-dimensional heat transfer model for GTAW process using finite element method coupled with a genetic algorithm based identification of uncertain input parameters. *Metallurgical and Materials Transactions A*, **Vol. 39A**(No. 11), 2698-2710.
- Bag, S. & De, A. (2009). Development of an efficient numerical heat transfer model coupled with genetic algorithm based optimization for the prediction of process variables in GTA spot welding, *Science and Technology of Welding and Joining*, **Vol. 14**, 333-345.
- Bag, S.; De, A. & DebRoy, T. (2009). A genetic algorithm assisted inverse convective heat transfer model for tailoring weld geometry. *Materials and Manufacturing Processes*, **Vol. 24**(No. 3), 384-397.
- Bag, S. & De, A. (2010). Probing reliability of transport phenomena based heat transfer and fluid flow analysis in autogeneous fusion welding process, *Metallurgical and Materials Transactions A*, **Vol. 41A**(No. 9), 2337 - 2347.
- Benyounis, K. Y., Olabi, A. G. & Hashmi, M. S. J. (2005). Effect of laser welding parameters on the heat input and weld-bead profile. *Journal of Materials Processing Technology*, **Vol. 165**, 978-985.
- Bonifaz, E. A. (2000). Finite element analysis of heat flow in single-pass arc welding. *Welding Research Supplements*, **Vol. 79**(No. 5), 121s-125s.
- Chande, T. & Mazumder, J. (1984). Estimating effects of processing conditions and variable properties upon pool shape, cooling rates, and absorption coefficient in laser welding. *Journal of Applied Physics*, **Vol. 56**(No. 7), 1981-1986.
- Cho, S. H. & Kim, J. W. (2002). Analysis of residual stress in carbon steel weldment incorporating phase transformation. *Science and Technology of Welding and Journal*, **Vol. 7**, 212-216.
- De, A. & DebRoy, T. (2005). Reliable calculations of heat and fluid flow during conduction model laser welding through optimization of uncertain parameters. *Welding Journal*, **Vol. 84**(No. 7), 101s-112s.
- De, A.; Maiti, S. K.; Walsh, C. A. & Bhadeshia, H. K. D. H. (2003). Finite element simulation of laser spot welding. *Science and Technology of Welding and Joining*, **Vol. 8**, 377-384.
- DebRoy, T. & David, S. A. (1995). Physical processes in fusion welding. *Reviews of Modern Physics*, **Vol. 67**, 85-112.
- Deng, D. (2009). FEM prediction of welding residual stress and distortion in carbon steel considering phase transformation effects. *Materials and Design*, **Vol. 30**, 359-366.

- Deng, D.; Murakawa, H. & Liang, W. (2007). Numerical simulation of welding distortion in large structures. *Computational Methods in Applied Mechanics and Engineering*, **Vol. 196**, 4613–4627.
- Frewin, M. R. & Scott, D. A. (1999). Finite element model of pulsed laser welding. *Welding Journal*, **Vol. 78**, 15-22.
- Goldak, J. A.; Chakravarti, B. & Bibby, M. J. (1984). A new finite element model for welding heat sources. *Metallurgical and Materials Transactions B*, **Vol. 15B**, 229-305.
- Gupta, O. P. (2002). Finite and boundary element methods in engineering. Oxford and IBH Publications, New Delhi, India.
- He, X.; Fuerschbach, P. W. & DebRoy, T. (2003). Heat transfer and fluid flow during laser spot welding of SS 304 stainless steel. *Journal of Physics D: Applied Physics*, **Vol. 36**, 1388-1398.
- He, X.; Elmer, J. W. & DebRoy, T. (2005). Heat transfer and fluid flow in laser micro welding. *Journal of Applied Physics*, **Vol. 97**, 084909:1-9.
- Hong, K.; Weckmann, D. C.; Strong, A. B. & Zheng, W. (2003). Vorticity based turbulence model for thermo fluids modeling of welds. *Science and Technology of Welding and Joining*, **Vol. 8**(No. 5), 313-324.
- Jung, G. H. & Tsai, C. L. (2004). Plasticity based distortion analysis for fillet welded thin plate t-joint. *Welding Journal*, **Vol. 83**, 177-187.
- Lee, M. Y. & Kim, J. W. (2004). On-line penetration depth measurement system using infrared temperature sensing in CO<sub>2</sub> laser welding. *Advances in Non Destructive Evaluation*, **Vol. 270-273**, 2308-2314.
- Lhospitalier, S.; Bourges, P.; Bert, A.; Quesada, J. & Lambertin, M. (1999). Temperature measurement inside and near the weld pool during laser welding. *Journal of Laser Applications*, **Vol. 11**, 32-37.
- Liu, J. T.; Weckman, D. C.; & Kerr, H. W. (1993). The effects of process variables on pulsed Nd:YAG laser spot welds: Part I. AISI 409 stainless steel. *Metallurgical and Materials Transactions B*, **Vol. 24**, 1065-1076.
- Mackwood, A. P. & Crafer, R. C. (2005). Thermal modelling of laser welding and related processes: a literature review. *Optics & Laser Technology*, **Vol. 37**, 99-115.
- Mazumder, J. & Steen, W. M. (1980). Heat transfer model for CW laser material processing. *Journal of Applied Physics*, **Vol. 51**(No. 2), 941-947.
- Mishra, S. & Debroy, T. (2005). A computational procedure for finding multiple solutions of convective heat transfer equations. *Journal of Physics D: Applied Physics*, **Vol. 38**, 2977-2985.
- Oreper, G. M. & Szekely, J. (1987). A comprehensive representation of transient weld pool development in spot welding operations. *Metallurgical and Materials Transactions A*, **Vol. 18A**, 1325-1332.
- Pitscheneder, W.; DebRoy, T.; Mundra, K. & Ebner, R. (1996). Role of sulfur and processing variables on the temporal evolution of weld pool geometry during multi-kilowatt laser beam welding of steels. *Welding Journal*, **Vol. 75**(No. 3), 71s-78.
- Pitscheneder, W.; Ebner, R.; Hong, T.; Debroy, T.; Mundra, K. & Benes, R. (1997). Experimental and numerical investigations of transport phenomena in conduction mode weld pools. *Proceedings of Fourth International Seminar on Numerical Analysis of Weldability*, pp. 379-395, ISBN, Graz- Seggau, September 1997, Austria.

- Price, K.; Storn, R. & Lampinen, J. (2005). *Differential Evolution – A Practical Approach to Global Optimization*. Springer, Berlin.
- Reddy, J. N. & Gartling, D. K. (2000). *The Finite Element Method in Heat Transfer and Fluid Dynamics*, CRC Press, Florida.
- Sahoo, P.; Debroy, T. & Macmillan, M. J. (1988). Surface tension of binary metal-surface active solute systems under conditions relevant to welding metallurgy. *Metallurgical and Materials Transactions B*, **Vol. 19**, 483-491.
- Storn, R. (1997). Differential evolution, a simple and efficient heuristic strategy for global optimization over continuous spaces. *Journal of Global Optimization*, **Vol. 11**, 341-359.
- Tanriver, U.; Longobardi, J.; Latham, W. P. & Kar, A. (2000). Effect of absorptivity, shielding gas speed, and contact media on sheet metal laser welding. *Science and Technology of Welding and Joining*, **Vol. 5**, 310-316.
- Teng, T. L.; Fung, C. P.; Chang, P. H. & Yang, W. C. (2001). Analysis of residual stresses and distortions in T-joint fillet welds. *International Journal of Pressure Vessels and Piping*, **Vol. 78**, 523-538.
- Trivedi, A.; Bag, S. & De, A. (2007). Three dimensional transient heat conduction and thermomechanical analysis for laser spot welding using adaptive heat source. *Science and Technology of Welding and Joining*, **Vol. 12**(No. 1), 24-31.
- Tzeng, Y. F. (1999). Pulsed Nd:YAG laser seam welding of zinc coated steel. *Welding Journal*, **Vol. 78**(No. 7), 238s - 244s.
- Tzeng, Y. (2000). Parametric analysis of the pulsed Nd:YAG laser seam-welding process. *Journal of Materials Processing Technology*, **Vol. 102**, 40-47.
- Zhao, H.; White, D. R. & DebRoy, T. (1999). Current issues and problems in laser welding of automotive aluminum alloys. *International Materials Reviews*, **Vol. 44**, 238-266.
- Zhang, W.; Roy, G. G.; Elmer, J. W. & DebRoy, T. (2003). Modeling of heat transfer and fluid flow during gas tungsten arc spot welding of low carbon steel. *Journal of Applied Physics*, **Vol. 93**(No. 5), 3022-3033.

IntechOpen



## **Laser Welding**

Edited by Xiaodong Na, Stone

ISBN 978-953-307-129-9

Hard cover, 240 pages

**Publisher** Sciyo

**Published online** 17, August, 2010

**Published in print edition** August, 2010

This book is entitled to laser welding processes. The objective is to introduce relatively established methodologies and techniques which have been studied, developed and applied either in industries or researches. State-of-the art developments aimed at improving or next generation technologies will be presented covering topics such as monitoring, modelling, control, and industrial application. This book is to provide effective solutions to various applications for field engineers and researchers who are interested in laser material processing.

### **How to reference**

In order to correctly reference this scholarly work, feel free to copy and paste the following:

Swarup Bag and Amitava De (2010). Computational Modelling of Conduction Mode Laser Welding Process, Laser Welding, Xiaodong Na, Stone (Ed.), ISBN: 978-953-307-129-9, InTech, Available from: <http://www.intechopen.com/books/laser-welding/computational-modelling-of-conduction-mode-laser-welding-process>

**INTECH**  
open science | open minds

### **InTech Europe**

University Campus STeP Ri  
Slavka Krautzeka 83/A  
51000 Rijeka, Croatia  
Phone: +385 (51) 770 447  
Fax: +385 (51) 686 166  
[www.intechopen.com](http://www.intechopen.com)

### **InTech China**

Unit 405, Office Block, Hotel Equatorial Shanghai  
No.65, Yan An Road (West), Shanghai, 200040, China  
中国上海市延安西路65号上海国际贵都大饭店办公楼405单元  
Phone: +86-21-62489820  
Fax: +86-21-62489821

© 2010 The Author(s). Licensee IntechOpen. This chapter is distributed under the terms of the [Creative Commons Attribution-NonCommercial-ShareAlike-3.0 License](#), which permits use, distribution and reproduction for non-commercial purposes, provided the original is properly cited and derivative works building on this content are distributed under the same license.

IntechOpen

IntechOpen